Ion-write micro-thermotics: programing thermal metamaterials at the microscale

Hwan Sung Choe[1,2†], Radhika Prabhakar[3†], Geoff Wehmeyer[4†], Frances I. Allen[1], Woochul Lee[2,5], Ying Li[6], Peidong Yang[5], Cheng-Wei Qiu[6], Chris Dames[4], Mary Scott[1,2], Je-Hyeong Bahk[3*], and Junqiao Wu[1,2*]

[1]*Department of Materials Science and Engineering, University of California, Berkeley, California 94720, USA*

[2]*Materials Sciences Division, Lawrence Berkeley National Laboratory, Berkeley, California 94720, USA*

[3]*Department of Electrical Engineering and Computer Science, University of Cincinnati, Cincinnati, Ohio 45221, USA*

[4]*Department of Mechanical Engineering, University of California, Berkeley, California 94720, USA*

[5]*Department of Chemistry, University of California, Berkeley, California 94720, USA*

[6] *Department of Electrical and Computer Engineering, National University of Singapore, Singapore, 117583*

[†] These authors contributed equally to this work.

*Authors to whom correspondence should be addressed, Electronic addresses: wuj@berkeley.edu and bahkjg@ucmail.uc.edu

Abstract

Considerable advances in manipulating heat flow in solids have been made through the innovation of artificial thermotic structures such as thermal diodes, camouflages and cloaks. Such thermal devices can be readily constructed only at the macro, centimeter scale by mechanically assembling different materials with distinct values of thermal conductivity. Rapidly growing needs in areas such as thermal management of microelectronics require these concepts to be extended to the microscale. Here, we demonstrate a monolithic material structure on which nearly arbitrary microscale thermal metamaterial patterns can be written and programmed. It is based on a single, suspended silicon membrane whose thermal conductivity is locally, continuously and reversibly engineered over a wide range (between 2 and 70 W/m-K at 300K) and with fine spatial resolution (10 ~ 100 nm) by focused ion irradiation. Our thermal cloak and rectifier demonstrations show how ion-written micro-thermotics can be used as a platform to create thermal metamaterials that control heat flow at the microscale.

Thermotic structures are heterogeneous systems designed to provide qualitatively new thermal functionalities that cannot be achieved in homogenous, natural materials. At the macroscale, advances in transformation thermodynamics theory have stimulated experimental demonstrations of thermotic devices to precisely route the heat flow in thermal cloaks (1; 2; 3), camouflages (4), inverters (2), concentrators (2), thermostats [??], and shields [??]. These macroscopic demonstrations utilize different materials with highly contrasting thermal conductivities (*e.g.* metals and polymers), mechanically integrated into a designed geometric pattern. Microscale versions of these thermotic devices would enable new thermal design capabilities for controlling heat flows in applications ranging from microelectronics or data storage to energy conversion systems. One previous approach to scale these thermal devices down to the microscale relies on drilling small holes in suspended crystalline membranes by nano-patterning using electron-beam lithography (5). These holes impart nearly zero thermal conductivity to the crystalline regions and enable the formation of binary composite thermal structures, similar to those of macroscopic devices; we refer to this configuration as "digital", because the thermal conductivity takes two discrete, fixed values in the composite. However, this approach is insufficient in general cases, and a different, "analog" configuration is needed where more than two? values, or even continuous variation of local thermal conductivity, are needed. For example, in order to implement a thermal cloak, there must be at least three distinct thermal conductivities available. However, mechanical integration of distinct materials at the microscale presents daunting technical challenges, and even if successful, mismatched thermal expansion and non-negligible thermal resistances at the interfaces between different materials would destroy the desired heat flow manipulation. Analog-like, continuously varied values of thermal conductivity could be mimicked by averaging over an area with different filling fractions of holes, but this effective-medium approach is fundamentally incompatible with micro length scales.

In this work, we develop a platform for ion-write micro-thermotics (IWMT), where a thin (~120 nm), suspended, single-crystal Si membrane is locally irradiated by a tightly focused (~ 1 nm) He$^+$ ion beam in a helium ion microscope (HIM) to create microscale patterns. Depending on the dose of the irradiation, the local thermal conductivity (κ) of Si can be suppressed by more than one order of magnitude from that of crystalline towards the amorphous phase, an effect that has been recently demonstrated in Si nanowires at room temperature (6). The continuous tuneability of κ and the monolithic nature of the composite eliminate the aforementioned issues arising from the "digital" approach. The thermal conductivity suppression is also reversible upon a modest thermal annealing in an N$_2$ environment, offering re-programmability of the IWMT. IWMT provides a versatile platform with which microscale thermal metamaterial patterns can be designed and written to reroute local heat flow and achieve desired thermal functions. For example, we show that IWMT enables thermal cloaking of objects three orders of magnitude smaller in size than in all previous demonstrations (2; 3).

Figure 1a illustrates the device structure that creates and characterizes the IWMT platform. The structure is based on the suspended micro-pad devices that were developed to measure thermal conductivity of individual nanotubes (7), nanowires (8; 9) and nanoribbons (10). A single-crystal Si membrane bridges two micro-pads that are suspended from the solid substrate by long and flexural SiN$_x$ arms. Here the major difference from previous suspended micro-pad devices is that, unlike in previous cases where the measured object is transferred to and bonded onto the two pre-formed pads by focused ion beam (FIB) processing, here the Si membrane is designed to be monolithically integrated into the two pads via the Si base (11). This design eliminates the thermal contact resistance between the membrane (the heat channel) and the pads (the heat source and drain). As shown in the Methods, convective and radiative heat losses from

the pads and membrane are also negligible. Serpentine Pt electrodes were fabricated onto both pads and were electrically isolated from the Si base with an SiN_x layer. The Pt electrodes serve as both micro-heaters and thermometers for the thermal characterization of the Si membrane. The Si membrane (120 nm) is thinner than the projected stopping distance (242 nm, with longitudinal straggle of 99 nm) of the 25 keV He^+ ions generated by the HIM (see SRIM simulation in Supplementary information), so that most of the irradiating ions pass through the Si membrane, leaving behind uniform lattice damage in the form of point defects of broken bonds and atomic interstitials and vacancies. The energy of the He^+ ions was chosen to be relatively low so as to maximize the nuclear stopping power (hence lattice damage) versus the electronic stopping power (12), albeit not too low in order to avoid unwanted doping of the Si membrane with He atoms.

After irradiation with the ion beam, the irradiated area appears darker in both optical (Fig.1b) and SEM (Fig.1c) images. Figure 1b shows an optical image of a suspended Si membrane, where two concentric circles were written with the ion beam. Figure 1c shows an SEM image of another pattern consisting of periodic pristine and heavily irradiated regions with a period of 60 nm. The tight focal spot size (~ 1 nm) of the ion beam and the small transverse straggle (see Supplementary information) allow a very fine spatial resolution (< 100 nm in general, or < 10 nm for doses < 10^{15} ions/cm²) of the features patterned onto the Si membrane. Transmission electron microscopy (TEM) analysis of the pristine (i) and irradiated (ii) regions, as shown in Fig. 1d, reveals that the heavily irradiated region becomes amorphous, in stark contrast to the single-crystal phase in the pristine material. Such microstructural change of the membrane lays the materials foundation for the device mechanisms of the IWMT platform, as analyzed in detail below.

Prior to device demonstration of the IWMT platform, we investigate the effects of He^+ ion irradiation on the thermal conductivity (κ) of the crystalline Si membrane. Figure 2a shows the variation of κ in response to the ion irradiation experimentally measured over a wide range of temperatures. Here the channel is uniformly irradiated by rastering the ion beam over the entire suspended part of the Si membrane between the micro-pads; the irradiation dose is calculated from the beam current, irradiation time and area. The thermal conductivity measurements were performed under a vacuum of < 10^{-7} Torr to minimize parasitic convection loss (see Methods for details).

The pristine Si membrane shows a typical, non-monotonic T-dependent κ, with a room-temperature value of 65±5 W/m-K, consistent with literature-reported values (13) for a single-crystal Si thin film of comparable thickness. We note that as these membranes are only lightly doped with a resistivity above 20 Ωcm, the electronic contribution to κ is negligible, and the measured κ is attributed almost entirely to phonon-mediated thermal conduction. With the increase in irradiation dose ranging from 2×10^{13} to 1×10^{18} ions/cm², a clear, monotonic suppression in $\kappa(T)$ is observed. For example, at a dose of 10^{18} ions/cm², the room-temperature κ and peak κ are reduced from those of the pristine Si by a factor of 30 and 33, respectively. It is worth noting that in addition to the overall suppression of κ, the peak of $\kappa(T)$ shifts gradually toward higher temperatures, indicating increasing scattering of phonons by defects and domains newly created in the crystal. The peak vanishes in the measurement temperature range (< 300K) for irradiation doses exceeding ~10^{17} ions/cm². Vanishing of the peak in $\kappa(T)$ corresponds to amorphization of the Si membrane.

The suppression of κ in Fig. 2a is quantitatively consistent with that in Ref. (6) where κ of irradiated Si nanowires was measured only at room temperature. In contrast, the κ suppression observed over the wide temperature range in this work offers much richer information regarding the suppression mechanism through the temperature trends and peak shifts measured. In addition, the suppression of the pristine κ value is less severe for the IWMT membrane (κ = 65 W/m-K for 120 nm film thickness) than for the previous Si nanowire geometry (50 W/m-K for 160 nm nanowire diameter) (6), which enables better heat transfer rates through the pristine region of the IWMT, an effect beneficial for heat flow control.

To further correlate the microstructure evolution of the material to the reduction in κ, we performed systematic high-resolution transmission electron microscopy (HRTEM) and selected area electron diffraction (SAED) analysis on the Si membranes after irradiation with different doses; representative results are shown in Fig. 2b. For the pristine sample, the analysis confirms that the membrane is perfectly single crystalline with the (100) plane parallel to the membrane plane. The membrane remains single-crystalline after irradiation up to 10^{16} ions/cm^2. Beyond this dose, an amorphous phase starts to form inside the crystalline Si matrix, and the amorphous phase becomes significant after 10^{17} ions/cm^2 irradiation. At ~ 10^{18} ions/cm^2, the membrane is completely amorphized, as seen from the corresponding SAED pattern where the diffraction spots are lost and only diffusive rings are measured. This gradual evolution from point defects to amorphization is consistent with previous demonstrations of ion-irradiation-driven amorphization in Si (14; 15).

This analysis indicates that the suppression of κ is dominated by phonon scattering from point defects and amorphous domains in the low and high dose irradiation regimes, respectively. The measured $\kappa(T)$ was fitted by adopting the conventional model that incorporates Umklapp scattering, defects, and boundary scattering using Matthiessen's rule and the Born-von Karman dispersion for acoustic phonons. The modeled $\kappa(T)$ is shown by the solid line in Figure 2a and is in good agreement with the experimental data. The fitting parameters for the impurity scattering are shown in the Supplementary information. These data show that focused ion irradiation is a powerful tool for engineering local thermal conductivity of crystalline materials from the single-crystal phase continuously to the amorphous level, and at a spatial resolution of ~ 100 nm for κ suppression by a factor of 30, or even below ~ 10 nm for κ suppression by a factor of 2 (see Supplementary information for spatial resolution discussion). Below we will also show that such engineering of κ is also largely reversible.

The ability of the IWMT platform to route heat flux using these fine features enables the construction of a range of microscale thermotic devices on the Si membrane, such as thermal shields, cloaks, concentrators, inverters and diodes. A thermal shield routes heat fluxes around an object via exquisite design of local thermal conductivity tensors, shielding the object from the external heat flux. A thermal cloak hides the object from far-field thermal detection, which requires the re-routing of heat flow around the object while also mandating that the total heat flow is unchanged by the addition of the cloak and object. One possible application of thermal shields and cloaks could leverage the fact that these thermotic devices minimize the temperature gradient in the object, allowing physically separated elements in temperature-compensating sensor circuits to experience the same temperature even in the presence of external heat flows. In addition, the total heat flow is unchanged by the presence of a thermally cloaked object, and therefore, objects such as circuit elements can be added and cloaked in a complex thermal system without changing the heat transfer rates away from heat-generating elements, opening up capabilities for modular or iterative thermal design. Thermal shield and cloak structures have

been theoretically designed using the Fourier law of thermotics and experimentally demonstrated on the macroscale (*e.g.* centimeters) using materials with contrasting thermal conductivity (2; 3). However, these macroscale thermal cloaks are much too large to control heat flows at the microscale. Our IWMT approach provides a monolithic platform on which the thermal shield and cloak can be readily constructed. Proving the function of these devices, however, requires a spatial mapping of temperature over the entire device area, and is challenging for these microscale devices. We employ thermoreflectance imaging (TRI) (16; 17; 18) to map the temperature, which offers higher spatial resolution and temperature sensitivity than infrared thermography.

TRI is a non-contact optical technique for measurements of temperature variation on a surface by taking into account changes in optical reflectivity from the surface at different temperatures (19; 20). The relative change in reflectivity (ΔR) from the mean optical reflectivity (R) of a sample is related to the change in temperature (ΔT) of the surface using the thermoreflectance coefficient (C_{tr}) as $\Delta R/R = C_{tr}\Delta T$ (21; 22; 23; 24). Since C_{tr} depends on factors such as the material, its surface roughness, and the wavelength of light used for the measurement, it needs to be well calibrated for each sample prior to the actual measurement. The illumination wavelength is chosen for maximum sensitivity, *i.e.* highest magnitude of C_{tr}, typically in the range of 400 to 800 nm, and is therefore suited for sub-micron imaging. TRI can also offer ultra-high-speed transient thermal characterization of 50 ns down to sub-ns. All TRI in this work is performed using blue light (~ 470 nm) illumination, most suited to Si [??]. The imaging process involves first determining C_{tr} of the thermal cloak using both steady state and transient measurements. Steady state measurements are used with the substrate supported the thermal cloak in order to find a reference C_{tr} which is then used to calibrate for the entire cloak using the transient measurement method (TransientCAL) developed for TRI of nanoscale features (25). The C_{tr} map thus obtained is used for mapping the temperature on the thermal cloak (see Methods for measurement conditions and setup and the Supplementary information for details).

In the first design of the thermal cloak, two concentric rings (hence called "bilayer" design) are patterned to create three distinct regions with different κ, as shown in Fig.3a; κ of regions i, ii and iii are designed to be 70, 40 and 2 W/m-K at room temperature, respectively. Our finite-element simulation (Fig.3a) shows that such a device would effectively shield the thermal flux around the central circle when it is temperature biased, with a nearly constant temperature distribution in the shielded region (see Methods). Such a device is written by the ion beam on the Si membrane (Fig.3b) following the design, and regions i, ii, and iii are created by irradiation with a dose of 0 (pristine), 5×10^{14}, and 1×10^{18} ions/cm^2, respectively. The temperature distribution of the device under thermal bias, mapped by the TRI technique (middle panel in Fig.3b), shows that indeed, the middle circular region appears as a plateau with nearly isothermal temperature distribution. Since the pristine region (region i) of the cloak has a higher thermal conductivity with a larger temperature gradient than the cloaked object, this indicates that the heat is mostly routed around the central region, as is required for thermal cloaking. Furthermore, out finite-element simulations (see Methods) using the experimentally measured κ reveal that the heat flow is changed by only 4% through the addition of concentric cloaking structures, and this heat flow is only very weakly dependent on the thermal conductivity of the object. Therefore, these combined observations prove the microscale cloaking capabilities of the thermotic device.

The performance of the thermal cloak can be further improved by adding finer structure in the design. Figure 3c shows the second device called the "quadlayer" design, in which two circular heat barriers instead of just one (as used in the first device) are fabricated to realize a

more uniform temperature distribution in the central area. This quadlayer device is designed with three distinct values of κ of 70, 30, and 2 W/m-K, which were realized on the IWMT platform by irradiation at 0, 2×10^{15}, and 10^{18} ions/cm^2, respectively. TRI mapping in Fig.3c shows an enhanced uniformity of the temperature distribution in the inner circle compared with the bilayer design. Both the bilayer and quadlayer devices utilize the finely structured local thermal conductivity of the IWMT to bend heat flow around the central object. These designs necessitate the continuous control of thermal conductivity and monolithic integration of different constituents as achieved in the IWMT. Obviously, the IWMT can be configured to construct other types of thermal devices as well. In the Supplementary information, a classical thermal rectifier is also demonstrated on the IWMT at 200K, where the thermal conductance differs by 2.4 % when the heat flow direction is reversed under a temperature bias of 30K.

Lastly, we show that the suppression of κ in the IWMT is also reversible and rewritable. As shown in Fig.4a, the room-temperature κ is suppressed relative to the original $\kappa_{pristine} = 65$ W/m-K to 55 W/m-K ($\approx 0.85\kappa_{pristine}$) by irradiation of 10^{14} ions/cm^2. A moderate anneal of the device in an N_2 gas environment at 300°C restores the suppressed κ to 62 W/m-K ($\approx 0.95\kappa_{pristine}$). For irradiation at higher doses, the suppression is greater and the recovery of κ is less. For example, after irradiation using 10^{15} ions/cm^2 (Fig.4b), κ is suppressed to 33 W/m-K = $0.51\kappa_{pristine}$, and annealing restores it to $\kappa = 60$ W/m-K = $0.92\kappa_{pristine}$. Importantly, after the initial annealing, the system appears to be locked into two stable states, such that subsequent, further treatments of irradiation and annealing under the same condition always set and reset κ between the low (33 W/m-K) and high (60 W/m-K) values. Therefore, akin to non-volatile resistive random-access memory, the initial irradiation serves as a forming process, and the subsequent annealing and irradiation can repeatedly erase and encode the thermal conductivity variation in the membrane.

In summary, a versatile platform is developed to reversibly write microscale thermal metamaterials, and using the platform, thermal cloaking is demonstrated at the microscale. The capability of controlling microscale heat flow using this platform opens opportunities to experiment with novel ideas for microscale thermal management. As the spatial resolution of the ion writing is much smaller than that of the phonon mean free path (MFP) in crystalline Si (~ 1 μm at room temperature and longer for lower temperatures (26)), sub-MFP-sized devices can also be written onto the IWMT, which are potentially able to ballistically route thermal phonon transport for exploring exotic thermal effects beyond the Fourier law (27). The gradual and controlled transition from the crystalline to amorphous phase in the IWMT also offers an ideal material system with which to test novel thermal conduction physics, such as the transition from thermal phonons to heat-carrying local vibration modes (or the so-called propagons and locons, respectively) (28). Using other ultra-thin materials such as graphene (29) as the membrane, an even wider range of modulation of thermal conductivity could be achieved, which would enable improved or new functions. In this sense, the ion-write micro thermotics demonstrated here has the potential to serve as a versatile platform with which to control heat flow at the microscale, akin to what nanofluidics does for fluids.

Author Contributions

J.W. conceived this project, H.S.C. and W.L. fabricated the suspended microdevices. H.S.C. and F.I.A. performed the HIM irradiation. M.S. performed HRTEM and SAED analysis. R.P. and J.B. performed the TRI experiments. G.W. and C.D. performed the simulation. H.S.C., R.P., G.W. and J.W. analyzed the data and drafted the paper. All authors discussed the results and contributed to writing the manuscript.

Additional information

Supplementary information is available online.

Methods

Device fabrication. Fabrication of the suspended micro-devices started with 6″ silicon-on-insulator wafers (SOI) (vendor: SOITEC). The silicon in the SOI was lightly p-doped, single-crystalline, with a resistivity of $20 \sim 30$ $\Omega{\cdot}cm$, hole concentration of $\sim 10^{15}$ cm^{-3}, (100) crystal orientation, and thickness of 200 ± 5 nm (thinned down to 120 nm in the final device). The buried silicon oxide layer and handle substrate were 200 ± 10 nm and 625 ± 10 μm thick, respectively. The silicon layer was patterned to define and form the silicon membrane below and between the two pads using photolithography (ASML 5500/300 DUV stepper) and a deep reactive ion etching process (SPTS ICP-SR deep reactive ion Etcher). A 300nm-thick, Si-rich, low-stress SiN_x layer was deposited by low-pressure chemical vapor deposition, followed by metallization of 2 nm Cr and 50 nm Pt for the electrodes using sequentially the stepper photolithography, sputtering, and lift-off. Afterwards, the SiN_x layer was patterned followed by reactive ion etching to expose the silicon membrane channel bridging the two pads. The wafer was cut into small chips of 9.2×9.2 mm in size, each containing 72 micro-devices with silicon membrane channels of various lengths. After defining the width of the silicon membrane channel using electron beam lithography (Crestec CABL-9000) and ICP etching (Oxford PlasmaLab 150 Inductively Coupled Plasma Etcher) using hydrogen bromide, the devices were finally released from the substrate by backside photolithography and selective deep reactive ion etching.

Irradiation. The suspended Si membrane was irradiated by He^+ ions using a Helium Ion Microscope (HIM, Zeiss ORION NanoFab). The incident ions were generated at the atomically sharp gas field-ionization source using a helium gas pressure of 2×10^{-6} Torr. The acceleration potential and beam spot size were set to 25 kV and ~ 1 nm diameter (10 μm aperture), respectively. The irradiation doses were controlled by varying the beam current, dwell time, and scan spacing. A 2 pA beam current, 1 μs dwell time, and 0.25 nm scan spacing were used for most of the irradiation processes, except for the highest doses (10^{17} and 10^{18} $ions/cm^2$), which used a 10nm spacing and 40 pA beam current (70 μm aperture). All patterns were designed and written using the NanoPatterning and Visualization Engine (NPVE) program from Fibics, Inc.

Thermal conductivity measurements. Thermal conductance (G) of the membrane was measured using the suspended micro-pad devices (9) placed in a cryostat with a vacuum chamber (pressure $\sim 10^{-7}$ Torr). Serpentine Pt electrodes pre-deposited on the two symmetric, suspended SiN$_x$ pads act as micro-heater and thermometer for the thermal measurements. G was measured by $G = (Q \times \Delta T_c) / [(\Delta T_h)^2 - (\Delta T_c)^2]$, where Q is the Joule heating power of the Pt micro-heater, and ΔT_h and ΔT_c are the temperature change of the hot and cold SiN$_x$ pads, respectively (30). When a DC current ($0 \sim 15$ μA) was flowing into the Pt micro-heater on the heating pad, ΔT_h and ΔT_c were simultaneously recorded by lock-in amplification of the Pt heater/thermometer resistance to an additional AC current (500 nA) applied to the micro-heater. The temperature coefficient of resistance (TCR) of the Pt heater/thermometer was pre-calibrated by quadratic fitting to its resistance as a function of global temperature prior to each measurement. The thermal conductivity measured in this study has a $< 5\%$ error, considering the errors of electrical measurements, as well as measurements of the sample dimensions.

TEM characterization of irradiated silicon membrane.

HRTEM data was taken in an FEI Titan at 300 keV from a test Si membrane sample. The sample was irradiated to the same dose as the devices, but was thinner (~ 30 nm) to allow for HRTEM imaging.

SAED data was taken in a Zeiss Libra TEM at 200 keV. Single devices with irradiated Si regions were mounted into an appropriate substrate using a low-temperature curing epoxy (200°C). Using the pristine crystalline region of each film, the sample was tilted until the electron beam direction coincided with the Si <100> direction. Then, diffraction data was acquired for each radiation dose.

Thermoreflectance Imaging. The thermoreflectance coefficient (C_{tr}) was calibrated for the suspended materials following the established TransientCAL method presented in (25), followed by their steady state thermal characterization. We used the TRI measurement setup (Microsanj NT-210B) in which an LED, through a microscope objective, illuminated the device under test (DUT) as it was biased, and a phase locked CCD camera captured the reflectance signals from the surface of the DUT (25; 31). A blue-light LED (wavelength ~ 470 nm), which is suited to silicon devices, was used throughout the experiment with a 100×, 0.6 NA (numerical aperture) microscope objective. Using substrate supported devices, C_{tr} of a SiN$_x$ region on the heater was first determined by steady state measurements and used for measuring ΔT on the active region (Si membrane). Using a 20 μs biasing pulse at 2% duty cycle, transient thermal images of the Si membrane cooling to ambient temperature were captured up to 670 μs, and used with the TransientCAL technique to obtain the C_{tr} map of the membrane. After the calibration procedure, one side of the membrane was heated for 20 μs at 10% duty cycle to obtain thermoreflectance signals at the steady state operating temperature. These were used with the C_{tr} map to extract the heat flow across the device and obtain the final temperature map on the surface of the Si membrane. Details of the TRI procedures used are available in the Supplementary information. The TRI measurements were done near room temperature. Convective heat loss from the device is estimated to be less than 10^{-8} W, much lower than the heat flux flowing in the Si membrane (about 10^{-4} W). Similarly, the temperature of the device was kept no more than ~ 350 K, and radiative heat loss is estimated to be less than 10^{-8} W.

Concept and simulation of thermal cloak. Two-dimensional (2D) thermal cloaks hide thermal information about a cloaked object from far-field measurements in the 2D plane. To illustrate thermal cloaking, consider one-dimensional heat flow through a medium of thermal conductivity

κ_m. If an object with a thermal conductivity κ_o is embedded in the medium, the steady-state temperature profile and heat flux vectors are modified. The goal of the thermal cloak is to restore the original one-dimensional temperature profile and heat flows outside of the cloaked region, such that thermal measurements do not reveal the presence of the cloaked object. Thermal cloaks achieve this restoration by routing the heat around the object without changing the magnitude of the total heat flow. Because the heat does not flow through the object, the object is ideally isothermal and the total heat flow is insensitive to κ_o.

Building on the designs of previously developed macroscopic thermal cloaks, we designed microscale thermal cloaks with bilayer and quadlayer designs. We consider cylindrical thermal cloaks patterned into a background material that is lightly irradiated to achieve an intermediate conductivity κ_m. Thin layers of heavily irradiated Si with a low thermal conductivity κ_I encircling the object provide insulation to prevent heat flow towards the cloaked object, while thicker cylindrical regions of pristine Si with a high thermal conductivity κ_P route the heat around the object. The rectangular background region has a length L along the direction of global heat flow x, width w in the orthogonal in-plane direction y, and thickness t. We perform 2D steady-state COMSOL simulations to find the temperature profiles and total heat flows through cloaked objects. We applied constant temperature boundary conditions at $x = 0$ and $x = L$ and adiabatic boundary conditions at $y = 0$ and $y = w$. We ensure mesh convergence by calculating the total heat flow in the x direction.

We evaluate the thermal cloaking efficiency using several cloaking metrics. First, we want the total heat flow Q from the hot edge at T_h to the cold edge at T_c with the cloaked object present to be identical to the total heat flow through a homogenous material with conductivity κ_m. Therefore, a perfect cloak would have $Q^* = \frac{QL}{\kappa_m tw(T_h - T_c)} = 1$. Second, we want Q to be insensitive to the value of the object thermal conductivity κ_o, demonstrating that the cloak is effective for many objects. One way to quantify this sensitivity is the dimensionless derivative $\delta = \frac{L}{wt(T_h - T_c)}\left(\frac{dQ}{d\kappa_0}\right)$, which should be small. Lastly, we want the dimensionless temperature gradient at the center of the object $g = \frac{L}{(T_c - T_h)}\frac{dT}{dx}$ to be smaller than unity, indicating that the cloak is effectively re-routing the heat around the object.

For our final designs demonstrated in Fig. 3, we selected the geometric parameters to optimize these cloaking metrics while ensuring that the object size was large enough to enable accurate TRI measurements, and that the highly irradiated section was as small as possible. The limit on the highly irradiated thickness arises because the TRI signal has artifacts due to irradiation-induced surface roughness. We found that our bilayer cloak design in Fig 3a with $\kappa_o = \kappa_m = 40$ W/m-K provides simulated cloaking values of $Q^* = 1.04$, $\delta = 0.06$, and $g = 0.50$. In particular, the small value of δ indicates that the measured Q is quite insensitive to the object's thermal conductivity, since in the absence of a thermal cloak this geometry has $\delta = 0.24$, a factor of eight higher. The simulations of the quadlayer cloak shown in Fig 3c displays similar cloaking capabilities ($Q^* = 1.11$, $\delta = 0.07$, and $g = 0.52$).
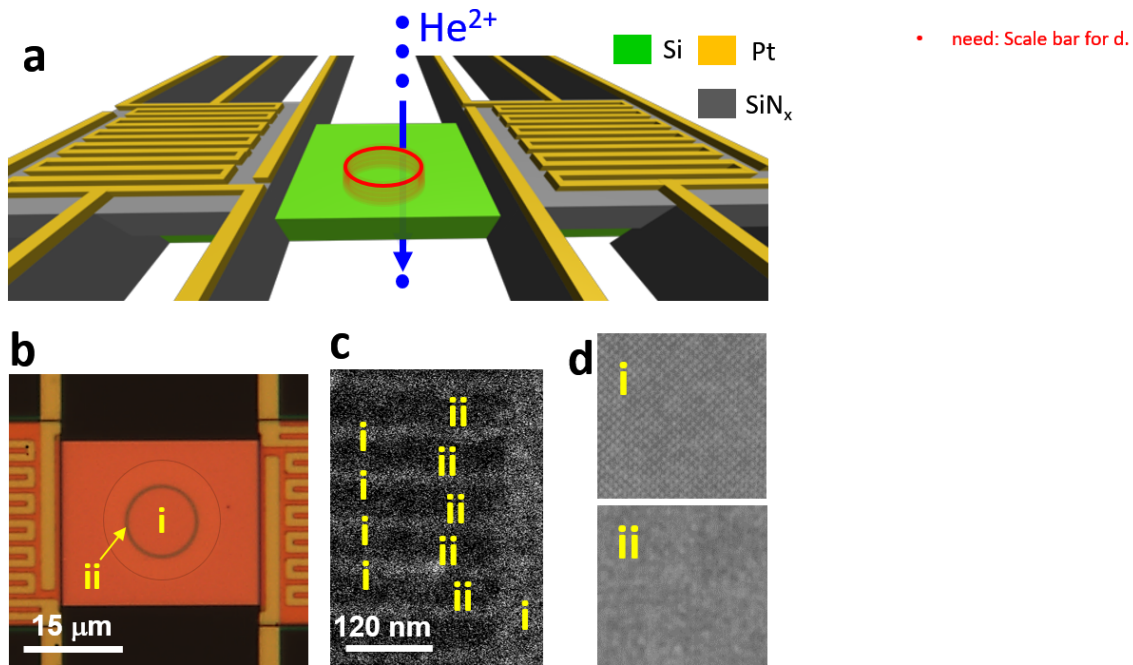
Figure 1 | The ion-write micro-thermotics (IWMT) platform created by site-selective He$^+$ ion irradiation. a, Schematic showing writing of local thermal conductivity in suspended single-crystal Si membrane using the He$^+$ ion beam. b, Optical image of a real device consisting of a suspended Si membrane bridging two micro-pads. The Si membrane is patterned with two concentric circles (region ii, darker reflection) at a dose of 10^{17} ions/cm^2. c, Zoom-in SEM image of another Si membrane where a periodic pattern of pristine (region i) / irradiated (region ii) is created with a period of 60 nm. d, HRTEM images of regions i and ii showing single crystal and amorphous Si phase, respectively.
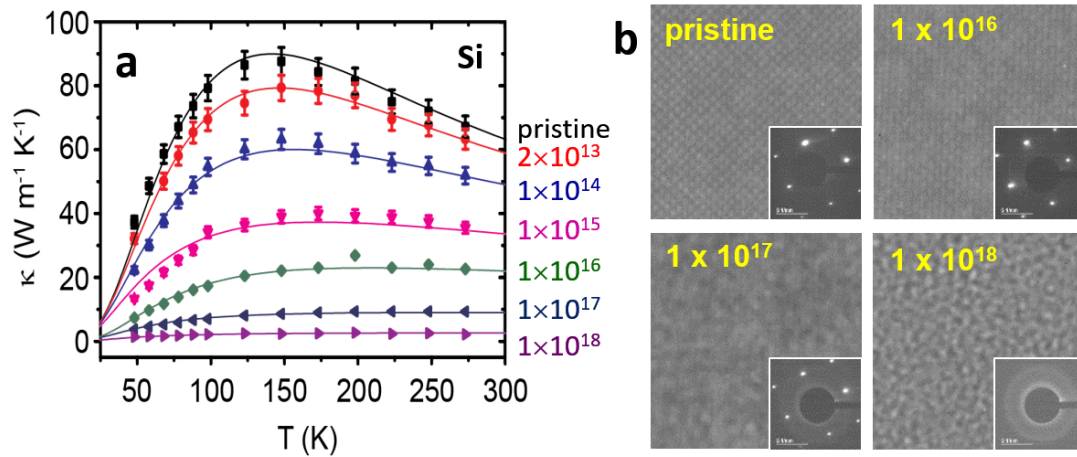
Figure 2 | Modulating thermal conductivity using He$^+$ ion irradiation. a, Temperature (T) dependent thermal conductivity (κ) of the Si membrane after irradiation for a wide range of irradiation doses (in ions/cm2). The curves are fits using a model including phonon scattering by defects, boundaries, and other phonons. b, HRTEM images of Si membranes after different doses of He$^+$ ion irradiation (in ions/cm2). Inset: SAED pattern corresponding to the different doses.
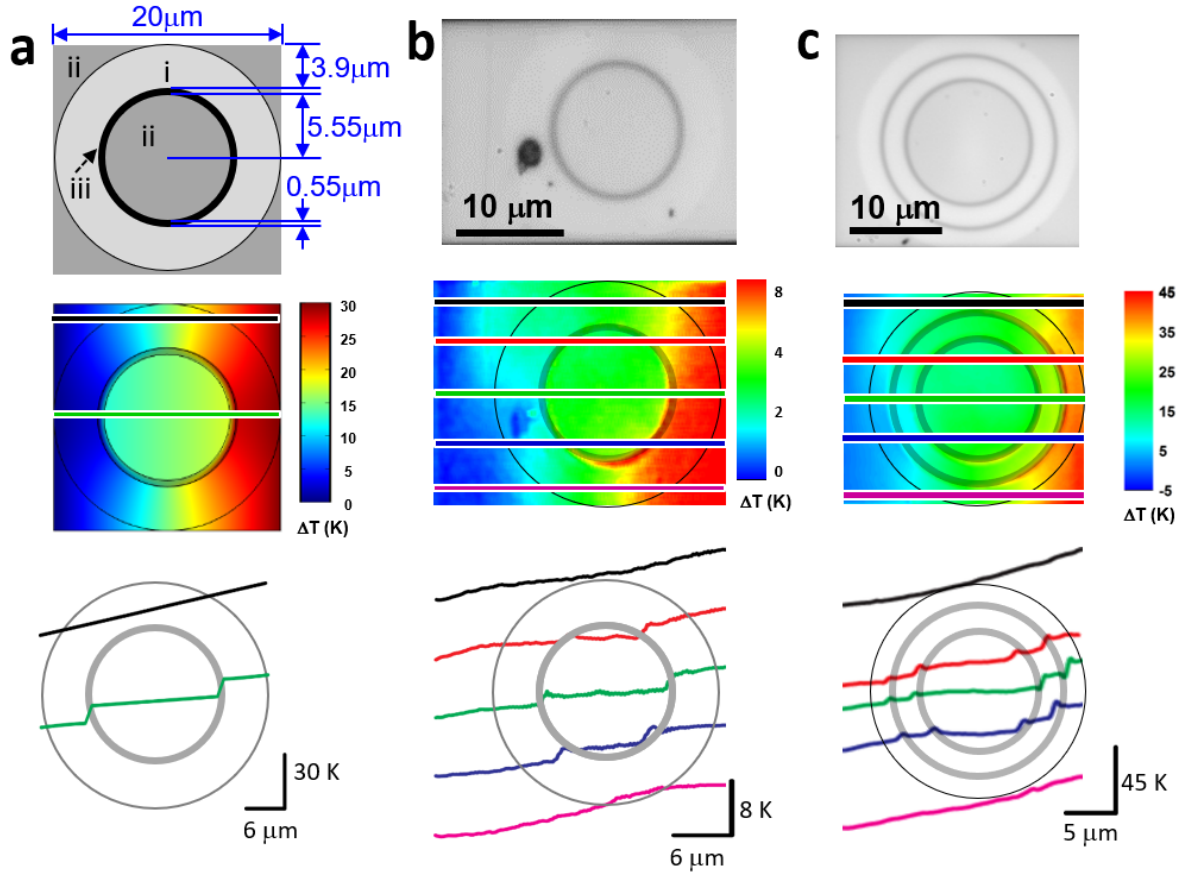
Figure 3 | Thermal cloaks demonstrated with the IWMT platform. a, Top to bottom: design of a bilayer thermal shield. The concentric i, ii, iii regions were irradiated with 0 (pristine), 5×10^{14}, and 1×10^{18} ions/cm² and have κ of 70, 40, and 2 W/m-K at room temperature, respectively; simulated temperature distribution of the design where the right and left edges are set at 330K and 300K, respectively; simulated temperature profile of the device along the straight lines indicated in the middle panel. b, Top to bottom: optical image of the bilayer thermal cloak realized on the IWMT platform following the design in a. The black dot is a dust particle contamination; temperature distribution of the device mapped by the thermoreflectance imaging (TRI) technique; measured temperature profile of the device along the straight lines indicated in the middle panel. c, Top to bottom: optical image of a quadlayer thermal cloak realized on the IWMT platform following the design in the Supplementary information; temperature distribution of the device mapped by the TRI technique; measured temperature profile of the device along the straight lines indicated in the middle panel. The three regions were irradiated using 0, 2×10^{15}, and 1×10^{18} ions/cm² and have κ of 70, 30, and 2 W/m-W, respectively.
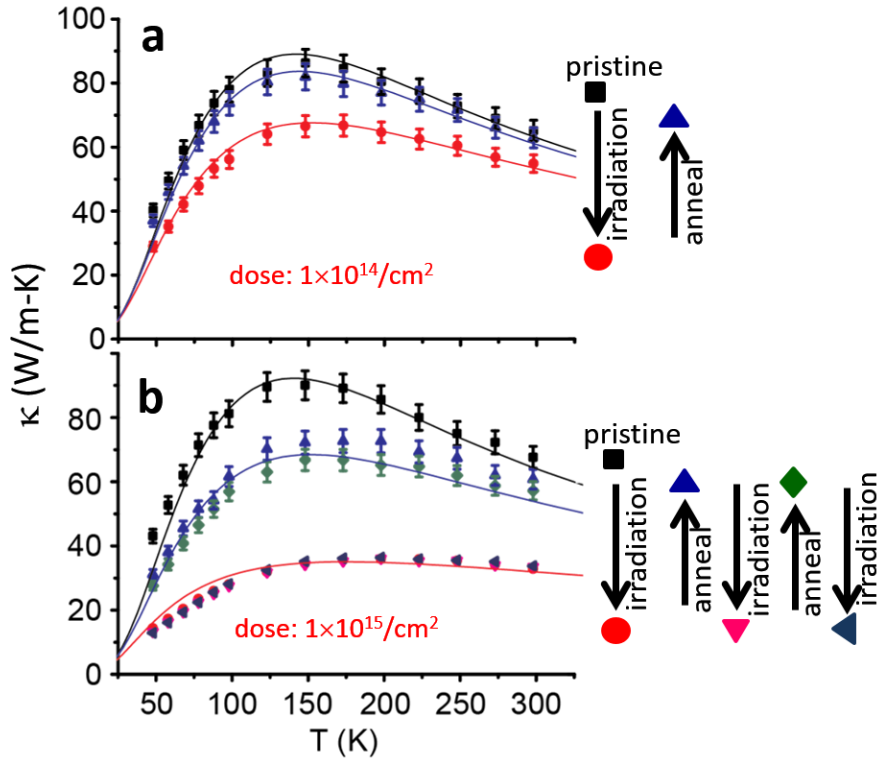
Figure 4 | Reversibility of the irradiation-engineered thermal conductivity. a, $\kappa(T)$ curves of a pristine Si membrane, after He$^+$ ion irradiation (dose=10^{14} ions/cm^2), and after anneal (300°C in N$_2$ for 2 hours). The anneal largely recovers the thermal conductivity. b. The same for He$^+$ ion irradiation at a higher dose (10^{15} ions/cm^2) and sequential, repeated anneal-irradiation steps, showing the reversibility of the process after the first anneal.

References

References

1. *Full Control and Manipulation of Heat Signatures: Cloaking, Camouflage and Thermal Metamaterials.* **Han, Tiancheng, et al.** 2014, Advanced Materials, Vol. 26, p. 1731.

2. *Heat Flux Manipulation with Engineered Thermal Materials.* **Narayana, Supradeep and Sato, Yuki.** 2012, Physical Review Letters, Vol. 108, p. 214303.

3. *Experimental Demonstration of a Bilayer Thermal Cloak.* **Han, Tiancheng, et al.** 2014, Physical Review Letters, Vol. 112, p. 054302.

4. *Structured thermal surface for radiative camouflage.* **Li, Ying, et al.** 2018, Nature Communications, Vol. 9, p. 273.

5. *Heat guiding and focusing using ballistic phonon transport in phononic nanostructures.* **Anufriev, Roman, et al.** 2017, Nature Communications, Vol. 8, p. 15505.

6. *Engineering the thermal conductivity along an individual silicon nanowire by selective helium ion irradiation.* **Zhao, Yunshan, et al.** 2017, Nature Communications, Vol. 8, p. 15919.

7. *Thermal Transport Measurements of Individual Multiwalled Nanotubes.* **Kim, P., et al.** 2001, Physical Review Letters, Vol. 87, p. 215502.

8. *Enhanced thermoelectric performance of rough silicon nanowires.* **Hochbaum, Allon I., et al.** 2008, Nature, Vol. 451, p. 163.

9. *Thermal Conductance of Thin Silicon Nanowires.* **Chen, Renkun, et al.** Physical Review Letters, Vol. 101, p. 105501.

10. *Anisotropic in-plane thermal conductivity of black phosphorus nanoribbons at temperatures higher than 100K.* **Lee, Sangwook, et al.** 2015, Nature Communications, Vol. 6, p. 8573.

11. *Investigation of phonon coherence and backscattering using silicon nanomeshes.* **Lee, Jaeho, et al.** 2017, Nature Communications, Vol. 8, p. 14054 .

12. **Nastasi, Michael, Mayer, James W. and Hirvonen, James K.** *Ion-Solid Interactions: Fundamentals and Applications.* New York : Cambridge University Press, 1996. p. 99.

13. *From the Casimir limit to phononic crystals: 20 years of phonon transport studies using silicon-on-insulator technology.* **Marconnet, Amy M., Asheghi, Mehdi and Goodson, Kenneth E.** 2013, Journal of Heat Transfer, Vol. 135, p. 061601.

14. *Ion-beam-induced amorphization and recrystallization in silicon.* **Pelaz, Lourdes, Marques, Luis A. and Barbolla, Juan.** 2004, Applied Physics Review, Vol. 96, p. 5947.

15. *Transmission electron microscopy study of ion implanation induced Si amorphization.* **Ruault, M. O., Chaumont, J. and Bernas, H.** 1983, Nuclear Instruments and Methods, Vol. 209/210, p. 351.

16. *Theoretical and experimental investigation of the thermal resolution and dynamic range of CCD-based thermoreflectance imaging.* **Mayer, Peter M., et al.** Journal of the Optical Society of America A, Vol. 24, p. 1156.

17. *Thermoreflectance based thermal microscope.* **Christofferson, James and Shakouri, Ali.** Review of Scientific Instruments, Vol. 76, p. 024903.

18. *Trasient thermal imaging using thermoreflectance.* **Maize, K., Christofferson, J. and Shakouri, A.** 2008. Annual IEEE Semiconductor Thermal Measurement and Management Symposium.

19. *Direct observation of nanoscale Peltier and Joule effects at metal insulator domain walls in vanadium dioxide nanobeams.* **Favaloro, Tela, et al.** 2014, Nano Letters, Vol. 14, p. 2394.

20. *Full-field thermal imaging of quasiballistic crosstalk reduction in nanoscale devices.* **Ziabari, Amikoushyar, et al.** 2018, Nature Communications, Vol. 9, p. 255.

21. *Calibration procedure for temperature measurements by thermoreflectance under high magnification conditions.* **Dilhaire, S., Grauby, S. and Claeys, W.** 2004, Applied Physics Letters, Vol. 84, p. 822.

22. *CCD-based thermoreflectance microscopy: principles and applications.* **Farzaneh, M., et al.** 2009, Journal of Physics D, Vol. 42, p. 143001.

23. *Quantitative thermal imaging by synchronous thermoreflectance with optimized illumination wavelengths.* **Tessier, G., Hole, S. and Fournier, D.** 2001, Applied Physics Letters, Vol. 78, p. 2267.

24. *Understanding the thermoreflectance coefficient for high resolution thermal imaging of microelectronic devices.* **Yazawa, K., et al.** 2013, Electronics Cooling Magazine, Vol. 2013, p. 10.

25. *Accurate thermoreflectance imaging of nano-features using thermal decay.* **Kendig, D., et al.** 2017. 16th IEEE Intersociety Conference on Thermal and Thermomechanical Phenomena in Electronic Systems (ITherm). p. 23.

26. *Impact of phonon surface scattering on thermal energy distribution of Si and SiGe nanowires .* **Malhotra, Abhinav and Maldovan, Martin.** 2016, Vol. 6, p. 25818.

27. *Crossover from incoherent to coherent phonon scattering in epitaxial oxide superlattices.* **Ravichandran, Jayakanth, et al.** 2014, Nature Materials, Vol. 13, p. 168.

28. *A method for distinguishing between propagons, diffusons, and locons.* **Seyf, Hamid Reza and Henry, Asegun.** 2016, Journal of Applied Physics, Vol. 120, p. 025101.

29. *Nanoscale thermal cloaking in graphene via chemical functionalization.* **Ye, Zhen-Qiang and Cao, Bing-Yang.** 2016, Phys. Chem. Chem. Phys. , Vol. 18, p. 32952.

30. *Measuring Thermal and Thermoelectric Properties of One-Dimensional Nanostructures Using a Microfabricated Device.* **Shi, Li, et al.** 2003, Journal of Heat Transfer, Vol. 125, p. 881.

31. *Thermoreflectance imaging of sub-100ns pulsed cooling in high-speed thermoelectric microscoolers.* **Vermeersch, J., et al.** 2013, Journal of Applied Physics, Vol. 113, p. 104502.

Supplementary information

Thermal conductivity modelling.

We model the thermal conductivity of silicon using the kinetic theory result $\kappa = \frac{1}{3}\sum_p \int C_{\omega,p} v_{\omega,p} \Lambda_{\omega,p} d\omega$, where p indexes the phonon polarization, ω is the phonon frequency, $C_{\omega,s}$ is the volumetric modewise specific heat, $v_{\omega,s}$ is the group velocity, $\Lambda_{\omega,s} = v_{\omega,s}\tau_{\omega,s}$ is the mean free path, and $\tau_{\omega,s}$ is the scattering time. This expression for κ assumes that the phonon dispersion relation and scattering rates are isotropic, an assumption which is commonly employed when modeling thermally isotropic materials such as silicon.

We use the Born-von Karman isotropic approximation for the silicon phonon dispersion relation $\omega = \omega_0 \sin\left(\frac{2k}{\pi k_0}\right)$, where k is the phonon wavevector, $k_0 = (6\pi^2 \eta_{PUC})^{1/3}$ is the Debye cutoff wavevector fixed by the experimental primitive unit cell density $\eta_{PUC} = 2.5 * 10^{23}\ \mathbf{m^{-3}}$ [S1], and $\omega_0 = 2v_s k_0/\pi$ is fixed by the experimental speed of sound v_s. We obtain v_s by an unweighted averaged of the measured speeds of sound along the [100], [110], and [111] directions and obtain $v_{s,LA} = 8973\ \mathbf{m/s}$ for the longitudion polarization and $v_{s,TA} = 5398\ \mathbf{m/s}$ for the two transverse polarizations [S1].

We use Matthiessen's rule to combine the phonon-phonon (Umklapp) scattering rate τ_U^{-1}, boundary scattering rate τ_B^{-1}, and impurity scatering time τ_I^{-1} as $\tau^{-1} = \tau_U^{-1} + \tau_B^{-1} + \tau_I^{-1}$. To model the phonon-phonon scattering, we use the relation $\tau_U^{-1} = P\omega^2 T \exp(-C_U/T)$ with the values $P = 1.9 * 10^{-19}\ \mathbf{s.K}$ and $C_U = 280\ \mathbf{K}$, which were obtained by a fit to temperature-dependent κ measurements of bulk silicon [S2]. The film thickness and nanoribbon aspect ratio is used to calculate the boundary scattering mean free path for a rectangular nanowire assuming fully diffuse boundary scattering [S3]. The form of the impurity scattering rate is $\tau_I^{-1} = A\omega^4$: for the bulk sample, $A = 2.5 * 10^{-45}\ \mathbf{s^3}$ .We obtain the impurity scattering strength A for each sample by fitting the measured $\kappa(T)$. We note here that A is the only free fitting parameter in the model.

Suppplementary Table 1 shows the values of the impurity scattering strength parameter A as a function of the ion dose. Here, A was determined by fitting to the data shown in Fig 2 of the main text. A increases monotonically with ion dose, representing the enhanced scattering with increasing point defect concentration. Supplementary Table 2 shows the values of A used in the reversibility studies of Fig. 4a,b.

Dose (ions/cm²)	Pristine	2×10^{13}	1×10^{14}	1×10^{15}	1×10^{16}	1×10^{17}	1×10^{18}
Impurity parameter A (10^{-45} s³)	5.3	8.5	19	59	190	910	5500

Supplementary Table 1: Impurity scattering parameters as a function of ion dose used in thermal conductivity modeling in Fig. 2. A is the only free fitting parameter in the model.

Dose (ions/cm^2)	1×10^{14}	1×10^{15}
Pristine impurity parameter $\boldsymbol{A}$ (10^{-45} s^3)	5.5	4.8
Irradiated impurity parameter $\boldsymbol{A}$ (10^{-45} s^3)	14	67
Annealed impurity parameter $\boldsymbol{A}$ (10^{-45} s^3)	7	13.5

Supplementary Table 2: Impurity scattering parameters for pristine, irradiated, and annealed samples shown in Fig. 4.

SRIM simulation of ion irradiation.

Monte Carlo simulations were performed using the stopping and range of ions in matter (SRIM) and the transport of ions in matter (TRIM) programs [S4] to evaluate and predict the lattice damage of the 25 keV He$^+$ ion irradiation into the 120-nm-thick Si membrane. Considering the spot size (~1 nm) of the focused He^{2+} ion beam, the irradiation dose was calculated by the accumulated number of the incident ions. The simulation results listed in Table S3 and S4 and Figure S1 show that, (1) most of (> 99%) the incident He$^+$ ions penetrate through the entire thickness of the suspended Si membrane without chemically doping the material, and (2) the defects introduced by the ion irradiation distribute uniformly across the thickness of the membrane. These SRIM and TRIM simulations indicate that the 25keV He$^+$ ion writing has a lateral resolution that depends on both the film thickness and the irradiation dose, ranging from 10 nm (for low doses $< \sim 10^{15}$) to ~100 nm (for high doses ~ 10^{18} ions/cm^2) for the 120-nm-thick Si membrane.

Irradiation dose (ions / cm^2)	Si vacancies / He ion	Backscattered He ions	Transmitted He ions
10^{16}	19.1	1%	99%
10^{17}	23.8	1.3%	98.7%
10^{18}	23.1	1.4%	98.6%

Supplementary Table 3: Simulated number of Si vacancies created per incident helium ion, and the percentage of backscattered and transmitted He$^+$ ions through the 120 nm-thick Si membrane. They add up to 100%, meaning that a negligible percentage of the He$^+$ ions stay embedded in the Si membrane.
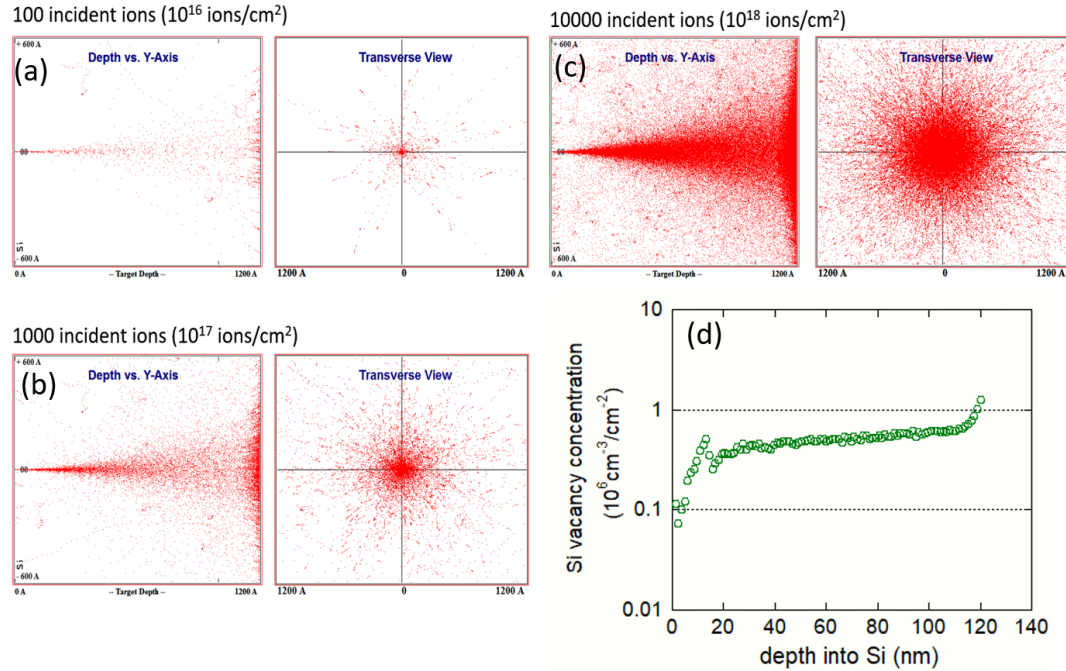
Figure S1: (a) – (c), SRIM simulated lattice damage when the 25keV He$^+$ ions are focused onto a single spot (< 1 nm). It can be seen that the lateral scattering of damage ranges from ~ 10nm to ~ 100nm, which defines the spatial resolution for the ion writing. (d) When the focused ion beam is rastering over the sample for laterally uniform irradiation, the simulated vacancies generated distribute uniformly over the membrane thickness. Here the vacancy concentration is given in cm^{-3}/cm^{-2}, meaning that the real vacancy concentration (in vacancies/cm^3) is this number multiplied by the irradiation dose (in ions/cm^2).

Thermoreflectance imaging (TRI) operation

The operation of the thermoreflectance imaging setup is briefly explained as follows.

The device under test (DUT) was biased for a certain time period and duty cycle. The LED light pulses were offset by a specific time delay relative to the device excitation. The CCD camera, exposure time of which was set up according to the device excitation, captured the reflected LED light from the device, thus storing reflected light variations from the hot and cold surfaces. Refer to Figure S2 for the timing diagram for this experiment. The system took a reference image at the LED delay of $t = 0$ with respect to the device excitation, which was used for image registration, alignment of the $t > 0$ images, and also for controlling the piezo stage for the xy and z drifts to prevent any long term drifting of the sample. Details of this setup and alignment procedures can be found in Reference [S5].
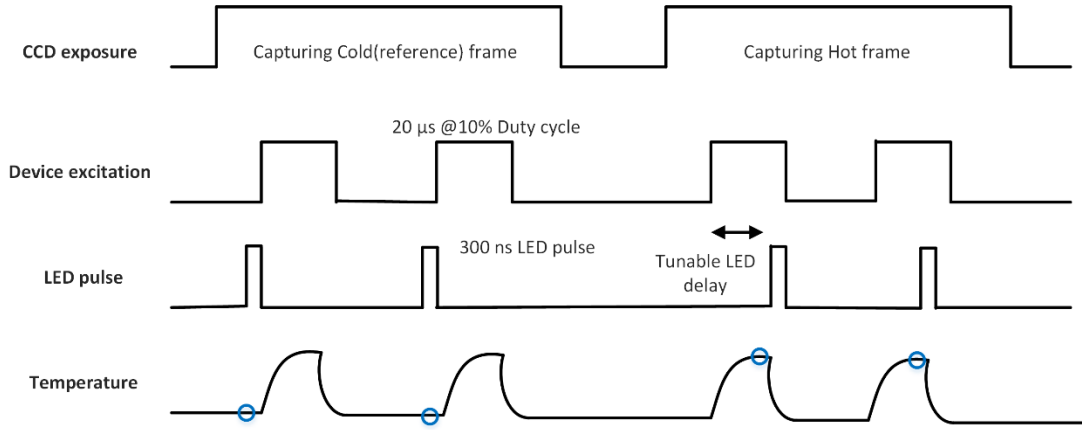
Figure S2: Timing diagram for capture of the reference (cold) image and the hot image. For our measurements, we used a 20 µs voltage pulse to bias the heaters and 300ns LED pulse for illumination. Blue circles show that the cold (reference) image was taken just before the device was turned ON, and the hot image was taken when the device reached steady state temperature after being powered ON. The CCD exposure time was adjusted to capture both the hot and cold images.

Thermoreflectance coefficient (C_{tr}) Calibration and temperature mapping.

C_{tr} calibration is done as a two-step process. First, steady state measurements are used for determining a reference C_{tr} on a substrate supported device. Second, transient measurements are used for obtaining a C_{tr} map on the Si membrane. Thermal images are then taken at steady state temperatures and combined with the C_{tr} map to obtain the temperature on the device.

Substrate supported devices with microscale features and larger allow simple global heating of device carrier / substrate while observing the temperature to obtain a C_{tr} map. Using a thermoelectric module or a heating stage, the device carrier is cycled between high and ambient temperatures to obtain the varying intensity 'hot' and 'cold' CCD frames.

For suspended MEMS devices, however, such a method for calibration is often not possible for the following reasons. First, isothermal heating of the device carrier does not allow for accurate temperature measurement on the membrane. The smallest thermocouples are 13-50 µm in size [S6], using them for temperature measurement on the suspended heater pads or membrane is not possible due to the fragile nature of the device. Second, even if we somehow manage to measure the temperature *in situ*, there will be considerable edge effect artifacts caused by global thermal expansion. Global thermal expansion gains considerable importance at larger magnifications and when the feature sizes are in the sub-micron range. There is a considerable expansion of the heating stage and the thermal expansion of the sample interferes with the piezo stage corrections, thus leading to drifts and artifacts [S5]. The smallest feature (ring) size in these devices is 500nm and 250nm for the bilayer and quadlayer metamaterial membrane, respectively. In such a case, local heating of the sample in question is most accurate.

We use the suspended heater pads for local heating of the Si membrane, with transient calibration technique [S5], which involves capturing of a series of thermoreflectance images of device cooling after it reaches a peak temperature and is turned off. However, as will be seen in the description of this method below, the transient calibration method does need a reference C_{tr} for the extraction of

the map. For this, we use a substrate supported device to determine C_{tr} of the reference region using steady state global heating. Keeping in mind the thermal expansion effects for submicron features, we choose a SiN_x region on the heater as the reference.

Figure S3(a) shows the CCD image of the Si membrane and the heaters. To observe the thermal decay via transient thermoreflectance imaging, both heaters were equally biased to uniformly heat the membrane using a 20 µs (2% duty cycle) voltage pulse. The thermal cloak thus reached its peak temperature at 20 µs and began to cool subsequently. Using a larger duration pulse, for instance, 100 µs to ~1ms, led to large amount of heating of the suspended device, causing twisting and bending of the suspension, thus affecting the focus and reflectance data. We therefore used small duration pulse at 2% - 20% duty cycle to avoid overheating and allow for enough cooling time. We collected ~11 transient thermoreflectance images from 20 µs to 670 µs with a time interval of 40 us. Each image was averaged for 1000 seconds to minimize the noise.

The SiN_x regions (blue and red regions on the heater in Figure S3(a)) were selected on the micro heaters. ΔT for this region could be ascertained by the C_{tr} value of this material. This was not known and must be determined *in situ* for accurate thermal characterization. Since a direct calibration of this material was not possible due to the suspended nature of the device. The SiN_x C_{tr} was determined using the substrate supported device (Si membrane and heater). The C_{tr} value obtained by cycling the device on substrate between high and low temperatures was -5×10^{-4} K^{-1}. Using this value of C_{tr}, we could see from the transient thermoreflectance cooling data that the ΔT of this region approached zero in a few hundred microseconds after the device is turned off. This is as expected and we used this value for transient calibration. The transient cooling temperatures for this region can be seen in Fig. S4 (a).

ΔT was determined using this C_{tr}. Assuming uniform heating, this ΔT was used as a reference to determine the thermoreflectance coefficients on a pixel by pixel basis to obtain a C_{tr} map using the TransientCAL method [S5]. Figure S3(b) shows the C_{tr} map of the membrane thus obtained.
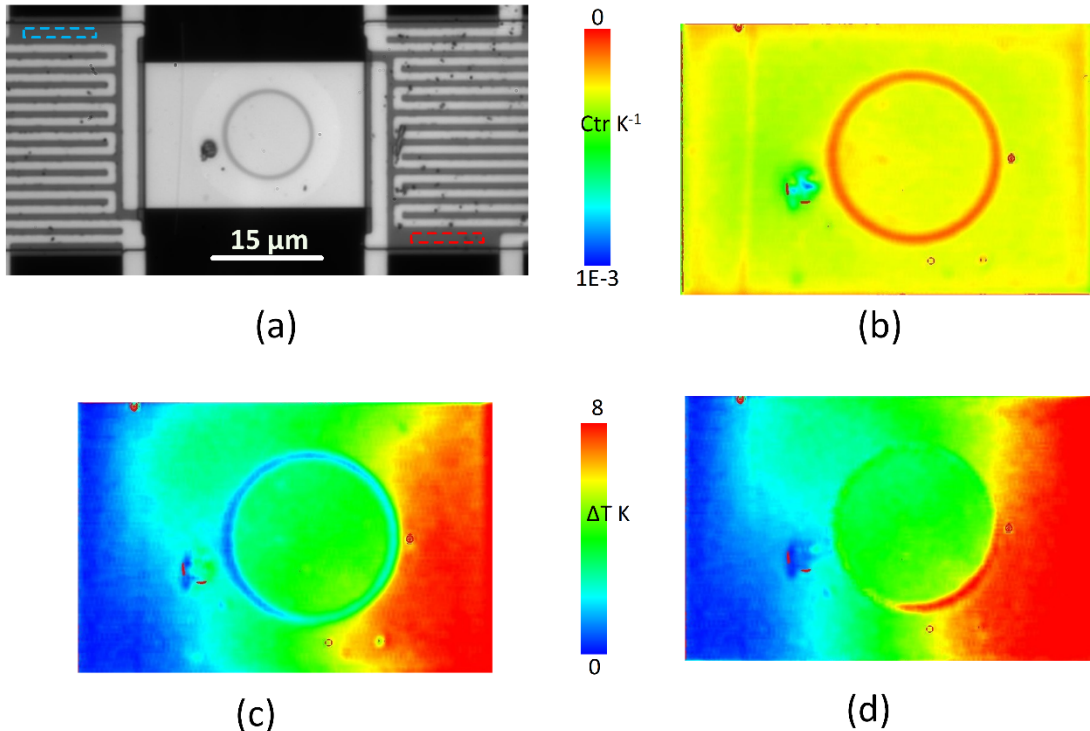

(a)

(b)

(c)

(d)

Figure S3: (a) CCD image of the suspended metamaterial Si membrane with the heaters. The dashed red and blue boxes show the SiN$_x$ region, the ΔT of which was used as a reference for the transient calibration. (b) C_{tr} map obtained from the transient calibration method. (c) Raw thermoreflectance signal from the membrane when heating the right side (here the average Si C_{tr} is applied to obtain the ΔT), and (d) the actual temperature obtained on the surface of the membrane after application of the C_{tr} map. It can be seen that application of the C_{tr} map corrects for artifacts obtained on submicron features leading to more accurate temperature information, and one C_{tr} cannot be used for the complete membrane, reaffirming the need for a pixel-by-pixel C_{tr} calibration.

Next, thermal characterization of the metamaterial membrane at steady state temperature was done by turning on one of the heaters to observe the heat flow across the membrane. Thermal images were taken at 20 µs (at 10% duty cycle) when the devices reached their peak temperature (as shown by the simulation in Fig.S4(b)). A longer time averaging (~3600 seconds) was used for the capture of the data to reduce the noise. The raw thermoreflectance data is plotted in Figure S3(c), whereas (d) shows the actual temperature map after application of the C_{tr}.
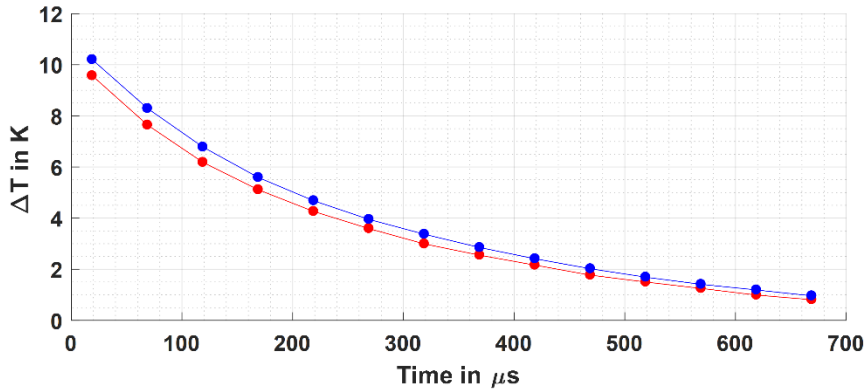
(a)
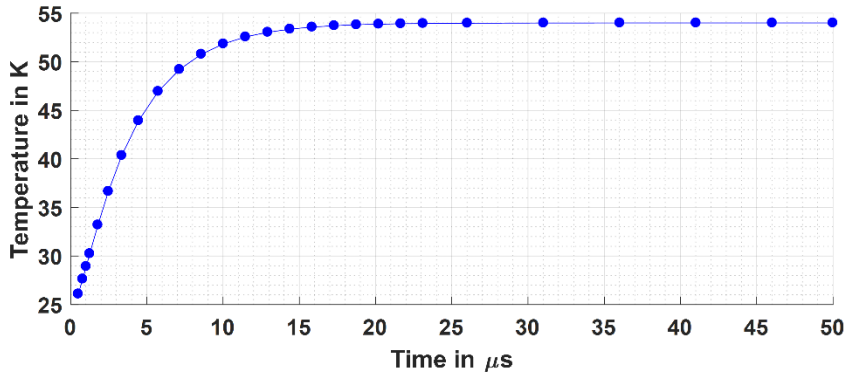
(b)

Figure S4: (a) Cooling of the SiN$_x$ regions on the heater pad. They were heated for 20 µs and then turned off. The highest temperature can be seen at ~19 µs when the heater is ON, followed by subsequent cooling with the lowest $\Delta T \sim 669$ µs. These temperatures were recorded using transient thermoreflectance imaging. (b) Simulation for the Si bilayer cloak shows that the device reaches a peak steady state temperature at ~20 µs. The FEM simulations were done in ANSYS for the device shown in in Fig. 1b using the thermal conductivities of 2, 40, 70W/m-K. This heating time was also used for measurements of the quadlayer cloak.

Demonstration of thermal rectification with IWMT

Thermal rectification, which occurs when heat flow experiences higher resistance in one direction than in the opposite direction, can be realized in a device called a thermal diode. Thermal diodes can find application, for example, in solid-state refrigeration cycle utilizing the magnetocaloric or electrocaloric effect. The thermal diode allows for strong thermal coupling when heat is pumped out of the refrigerator, while partially blocking undesirable heat backflow into the refrigerator during other portions of the cycle [S7]. One way to realize the thermal rectification is a "junction thermal diode" consists of two segments with thermal conductivities $\kappa(T)$ that have different temperature trends [S8].

The Si membrane in the IWMT can be irradiated with different doses to form a junction thermal diode. As shown in Fig. S5(b), the membrane was irradiated in the two segments with 10^{14} and 10^{18} ions/cm^2 doses, which provided a ratio in κ of 28.5, for maximal thermal rectification at 200K. A thermal rectification ratio of 2.4% was observed at 200K with 30K temperature bias of the device, as shown in Fig. S5(c). Fitting of the results in Figure S5(c) yields $\boldsymbol{\gamma = 0.16\,\Delta}$, where $\boldsymbol{\gamma}$ and Δ are thermal rectification ($\left|\frac{Q_{LR}-Q_{RL}}{Q_{LR}}\right|$) and dimensionless thermal bias ($\frac{T_H-T_C}{\frac{1}{2}(T_H+T_C)}$), respectively, as shown in Fig.S5(d). Here the subscription "L" and "R" stand for the left and right side, respectively, and "H" and "C" stand for the hot and cold side, respectively.
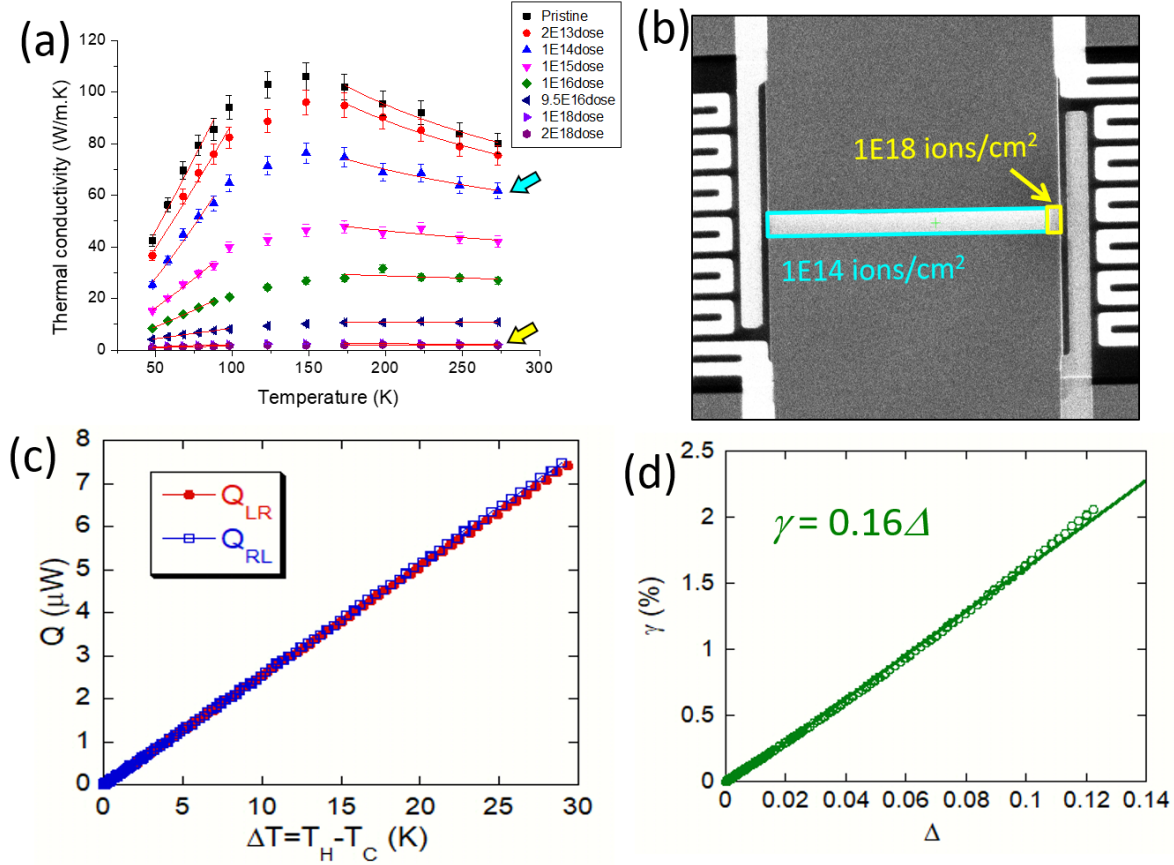
Figure S5: A thermal diode created by selective He^{2+} ion irradiation. (a) Thermal conductivity of the Si membrane Vs. temperature for various irradiation doses. Arrows show the two doses that are used for irradiation. (b) SEM image of the selectively irradiated Si membrane creating two segments of 10^{14} and 10^{18} ions/cm^2 doses, respectively. (c) Heat flow through the device (Q) as a function of temperature bias (ΔT). blue (red) data corresponds to the case of heat flow direction from right (left) to left (right). (d) thermal rectification, γ, as a function of dimensionless thermal bias (Δ).

Supplementary information references

[S1] C. Dames and G. Chen, J. Appl. Phys. 95, 682 (2004).

[S2] F. Yang and C. Dames, Phys. Rev. B 87, 035437 (2013).

[S3] A. K. McCurdy, H. J. Maris, and C. Elbaum, Phys. Rev. B 2, 4077 (1970).

[S4] The Stopping and Range of Ions in Matter, http://www.srim.org/

[S5] D. Kendig, G. Hohensee, E. Pek, W. Kuang, K. Yazawa and A. Shakouri, Accurate thermoreflectance imaging of nano-features using thermal decay, in 16th IEEE Intersociety

Conference on Thermal and Thermomechanical Phenomena in Electronic Systems (ITherm), pp. 23, 2017.

[S6] J. Christofferson, K. Maize, Y. Ezzahri, J. Shabani, X. Wang and A. Shakouri, Journal of Electronic Packaging, 130, 041101 (2008).

[S7] Geoff Wehmeyer, Christian Monachon, Tomohide Yabuki, Junqiao Wu and Chris Dames, Applied Physics Review, 4, 041304 (2017).

[S8] C. Dames, J. Heat Transfer, 131, 061301 (2009)